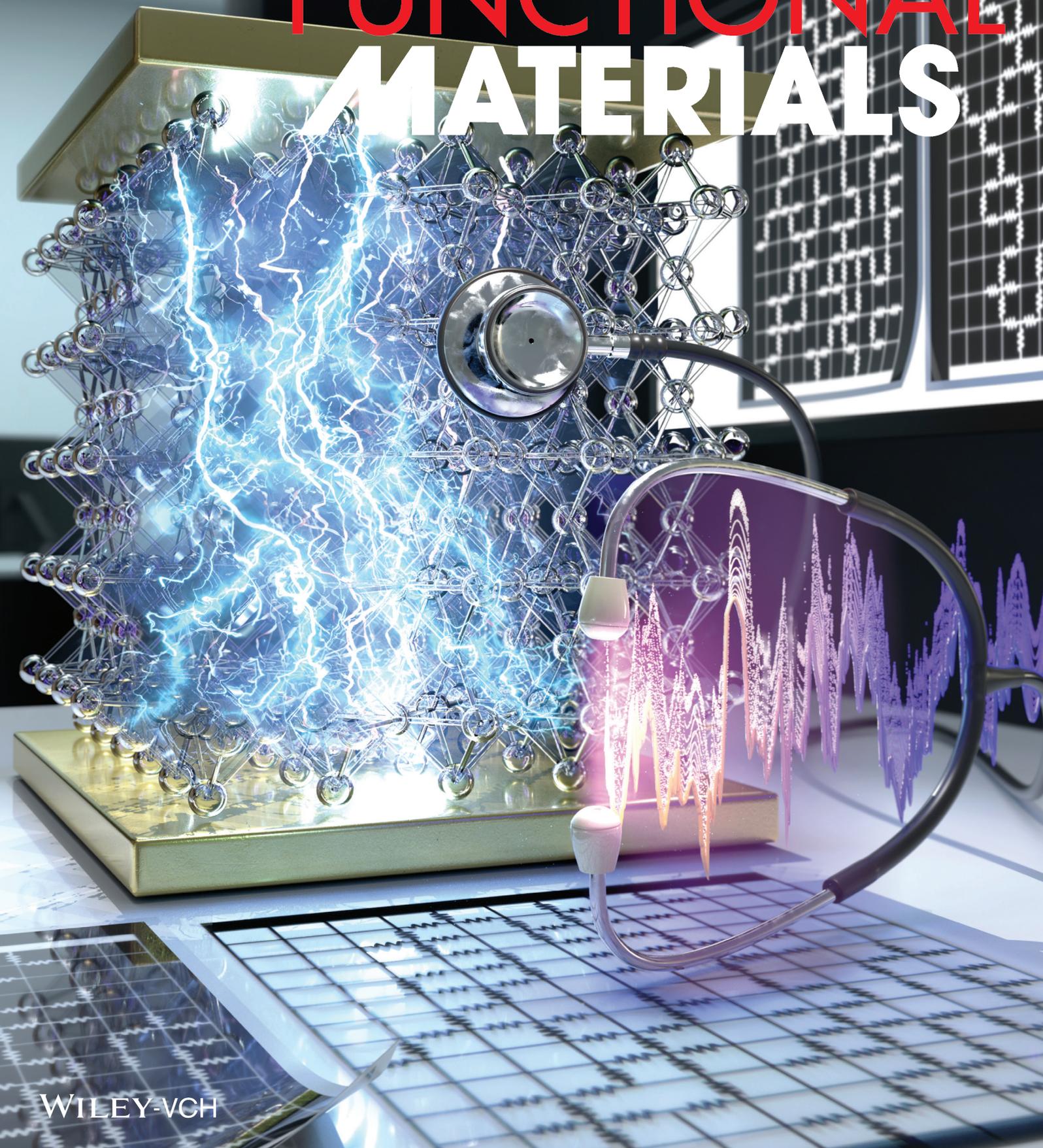# ADVANCED
FUNCTIONAL
MATERIALS

Resistive Switching by Percolative Conducting Filaments in Organometal Perovskite Unipolar Memory Devices Analyzed Using Current Noise Spectra

Heebeom Ahn, Keehoon Kang,* Younggul Song, Woocheol Lee, Jae-Keun Kim, Junwoo Kim, Jonghoon Lee, Kyeong-Yoon Baek, Jiwon Shin, Hyungbin Lim, Yongjin Kim, Jae Sung Lee,* and Takhee Lee*

Organometal halide perovskites have emerged as potential material systems for resistive memory devices besides their outstanding optical and electrical properties. Although halide-perovskite resistive memory has the advantage of operating with a low voltage and large on/off ratio, random distribution in operation voltage remains a challenge in memory application. This stochastic operation characteristic is due to the random formation of conducting filaments that cause resistance fluctuations in the material. Therefore, it is essential to investigate the formation and dissolution of conducting filaments and their structure. However, direct observation of a nanoscale filamentary structure is often challenging. Moreover, detailed studies of conducting filaments in halide-perovskite materials have rarely been reported. By employing a scaling theory with a fractal structure, this study investigates the geometric structures and dynamics of conducting filaments formed in organometal halide perovskite through current noise analysis. The temperature-dependent electrical properties and current noise demonstrate the role of ion migration in the formation of conducting filaments. The findings could enhance the understanding of the resistive switching phenomena of perovskite resistive memory devices in terms of percolative conducting filaments. Thus, providing a route for achieving a stable memory operation by controlling the relevant structure and dynamics of the switching processes.

H. Ahn, Y. Song, W. Lee, J.-K. Kim, J. Kim, J. Lee, K.-Y. Baek, J. Shin, H. Lim, T. Lee
Department of Physics and Astronomy
and Institute of Applied Physics
Seoul National University
Seoul 08826, Korea
E-mail: tlee@snu.ac.kr
K. Kang, Y. Kim
Department of Materials Science and Engineering
Yonsei University
Seoul 03722, Korea
E-mail: keehoon.kang@yonsei.ac.kr
J. S. Lee
School of Physics
Korea Institute for Advanced Study (KIAS)
Seoul 02455, Korea
E-mail: jslee@kias.re.kr

1. Introduction

Organometal halide perovskite has attracted significant attention as a material for various device applications, such as solar cells, light-emitting devices, and other electronic devices.[1–7] For electronic devices, organometal halide perovskite can be employed as nonvolatile resistive memory owing to its several advantages, such as low cost and solution-processability, high on/off ratio, and small switching power.[8–12] For example, a resistive memory device with a high on/off ratio of 10^9 using $MAPbCl_xI_{3-x}$ has been reported.[13] Additionally, a single crystalline $CsPbBr_3$ device with a small operation power of 30 nW has been presented.[14] In our previous study, we have demonstrated a methylammonium lead iodide ($MAPbI_3$) unipolar resistive memory device with a high on/off ratio of 10^8.[15] Although several studies have focused on the search for different halide-perovskite structures applicable to resistive memory devices and enhancing their performance, there are only a few studies on mechanistic investigation of their switching properties. Various mechanisms have been proposed for the resistive switching phenomenon of organic materials and metal oxides,[16,17] but many studies have suggested the formation and rupture of conducting filaments as the origin of resistive switching phenomena in organometal halide perovskite.[9,12,18–20] There is a consensus in the community that iodine vacancy with the lowest activation energy of migration plays a significant role in resistive switching.[12,18,21,22] Since these mobile point-defects are abundant in the material due to their low formation energy, metal ions from electrochemically active electrodes, such as Ag, can easily migrate to form a metallic filament through a redox reaction,[9,23] or vacancies can aggregate to form conductive clusters; thus, creating conducting filaments.[12,18–20]

By setting compliance current or controlling operation voltage, the growth of conducting filament can be controlled, which may lead to multistate operation in a resistive memory. Many studies have reported various intermediate resistance

**ADVANCED
SCIENCE NEWS**

www.advancedsciencenews.com

**ADVANCED
FUNCTIONAL
MATERIALS**

www.afm-journal.de

states (IRSs) in the organometal perovskite memory devices. However, the nature of different IRSs, which is related to the structure of conducting filaments in the material, has rarely been investigated. Moreover, a random structure of conducting filaments results in cycle-to-cycle and device-to-device variations in the perovskite memory devices. Therefore, understanding and controlling the structures of conducting filament is a key factor for determining the device's performance.[24,25] Several attempts have been made to observe and understand the properties of this filamentary structure using transmission electron microscopy.[26–29] However, it is not easy to observe the nanoscale structure and their 3D interconnection in conducting filaments directly.[30,31]

On the other hand, current noise analysis can be a powerful tool for probing the current distribution in a resistive medium. This method is indirect but simple, noninvasive, and can also provide statistical and microscopic insight into the charge transport phenomena. Current noise gives information about the origin of the current fluctuation in charge transport.[32,33] For example, noise analysis was used to figure out a trap distribution inside the channel material of field-effect transistors and at interfaces of light-emitting diodes.[34,35] Additionally, the magnitude of current noise is sensitive to the geometry of the current path; it has been applied to study conducting filaments in resistive memory devices through scaling analysis.[32,36,37] In this study, we observe and systematically analyze the noise scaling in various resistance states in perovskite unipolar resistive memory devices consisting of MAPbI$_3$ thin film as the active layer and a pair of symmetrical Au electrodes. By

employing the model of percolation clusters with fractal geometry, the scaling behavior could be correlated to conducting filament with particular structures with a fractal dimension in an organometal perovskite. We investigate how the current fluctuation of conducting filaments occurs at different temperatures through the current noise measurement in the time domain. The study on conducting filament geometry in perovskites will contribute to an understanding of each resistance state in the material, leading to stable resistive memory operations based on perovskite materials.

2. Results and Discussion

Figure 1a shows the schematics of the perovskite resistive memory device. First, Au (50 nm)/Ti (5 nm) was deposited as the bottom electrodes on a SiO$_2$/Si substrate using an electron beam evaporator. Then, the MAPbI$_3$ perovskite film was deposited through a simple one-step spin-coating with a non-halide lead precursor, lead acetate (PbAc$_2$) mixed with methyl-ammonium iodide (MAI). The structure of MAPbI$_3$ perovskite is shown in the inset of Figure 1a. After annealing the film, Au (50 nm) was deposited for the top electrodes to form 1 × 8 cross-bar array memory devices. As a result, memory cells with a size of 50 μm × 50 μm were fabricated (see Experimental Section for more details). Figure 1b shows the cross-sectional scanning electron microscope (SEM) image of a memory cell. It shows a well-defined MAPbI$_3$ perovskite memory layer with a thickness of about 200 nm without any noticeable penetration
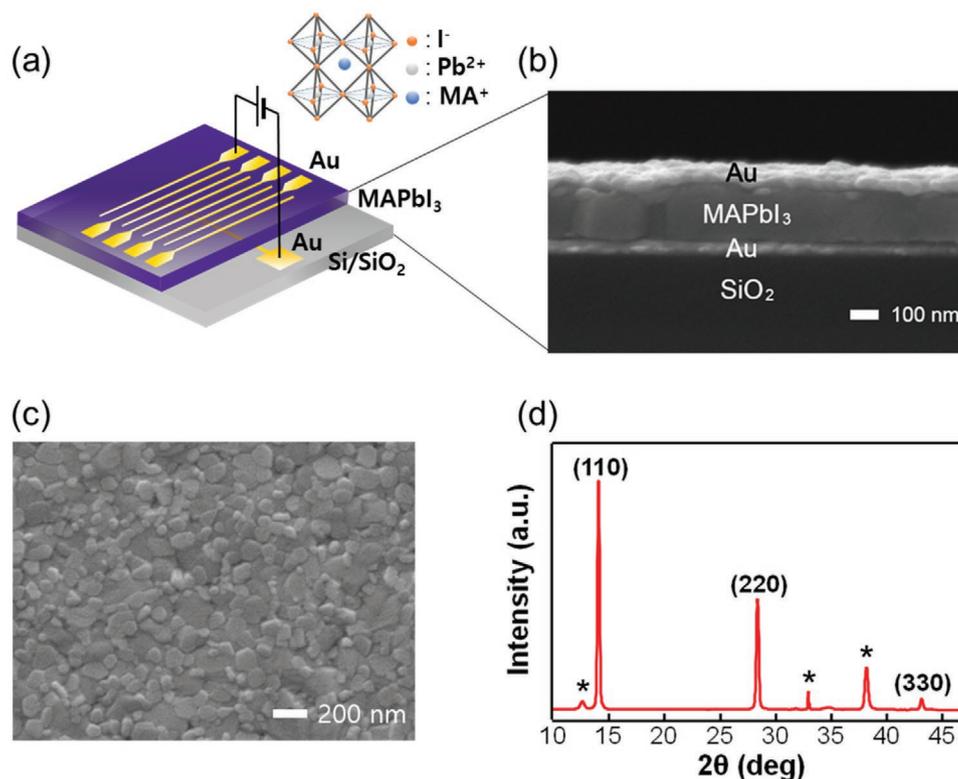

Figure 1. a) Schematic of the MAPbI$_3$ organometal perovskite resistive memory device. The crystal structure of MAPbI$_3$ is shown. b) Cross-sectional SEM image of a perovskite resistive memory device. c) SEM image of a MAPbI$_3$ thin film showing film morphology. d) XRD data of a MAPbI$_3$ thin film.
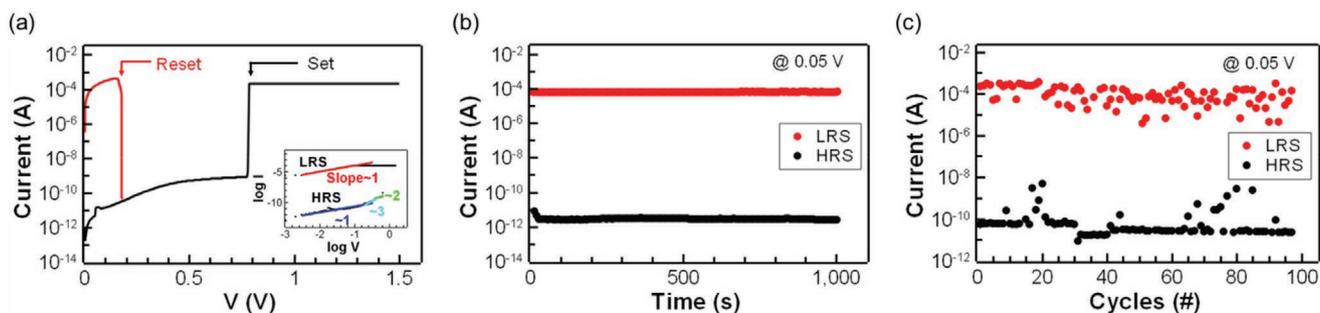
2107727 (2 of 9)

Figure 2. a) Representative current-voltage curve of a MAPbI$_3$ organometal perovskite resistive memory device. Inset presents the log-log plot of the same data. b) Retention test data and c) endurance-cycling data of a perovskite resistive memory device.

of metals into the layer. The SEM image of the MAPbI$_3$ perovskite film surface indicates a uniform film with a grain size of less than 100 nm (Figure 1c). According to X-ray diffraction (XRD) data for MAPbI$_3$ perovskite film on a silicon substrate shown in Figure 1d, sharp peaks corresponding to (110), (220), and (330) appeared, suggesting the formation of a tetragonal phase perovskite film.[38] Additionally, a small peak observed at 12.5° indicates residual PbI$_2$, which has not been converted to perovskite.[39] These XRD results demonstrate that a highly crystalline perovskite film with few remaining precursors was obtained. The 33° peak and 38.1° peak are seen due to Si and Au bottom electrodes, respectively.[40,41]

Figure 2a shows the representative current-voltage (I–V) curve of MAPbI$_3$ perovskite memory devices. As previously reported, MAPbI$_3$ perovskite memory devices showed unipolar resistive switching that could be set and reset at the same voltage polarity.[15] To prevent irreversible electrical breakdown, a compliance current of 20 μA was applied during the set process. Initially, the pristine memory device is in the high resistance state (HRS), and a relatively high voltage of near 3 V was required for forming process (see Figure S2, Supporting Information). Note that the electroforming process is a characteristic found in resistive memory devices that operate through filamentary switching.[31,42] The memory device switched to a low resistance state (LRS) at about 1 V (set voltage) and returned to HRS at about 0.4 V (reset voltage). The set and reset voltage values have a finite distribution, as can be discovered from repeated measurements (see Figure S4, Supporting Information). The on/off ratio determined as the ratio between the currents of HRS and LRS measured at 0.05 V was found to be as high as 3×10^7. The inset in Figure 2a shows the same I–V curve on the log-log scale with curve fittings, which can provide detailed information on the physical processes related to electrical conduction. In HRS, the ohmic behavior owing to intrinsic charge carriers in MAPbI$_3$ can be fitted to a slope of 1 in the low voltage region of the I–V curve. Trap-limited space charge limited current (SCLC) (slope > 2) and trap-free SCLC (slope of about 2) sequentially appeared when the voltage was gradually increased. However, LRS exhibited ohmic conduction (slope of about 1) in the entire voltage range. It was observed that LRS showed metallic conduction whose conductivity decreases with temperature.[15]

Generally, filamentary memory devices accompany an electroforming process, which requires a higher voltage bias than typical memory operation voltages to initiate the formation

of conducting filaments. Similar to other unipolar resistive switching systems with similar electrical transport properties (e.g., binary oxide and oxide perovskite memory devices),[28,37,43,44] it is assumed that a metallic conducting filament forms during the set process and ruptures in the reset process, resulting in the resistive switching in our devices. It has been proposed that conducting filaments are formed through iodine-vacancy migration/aggregation, which has the lowest activation energy of migration among the constituent ions of MAPbI$_3$.[12,18,21,22] Similar to the role of oxygen vacancies in metal-oxide materials, such as NiO$_x$, SrTiO$_x$, and TiO$_x$, the iodine-vacancy-rich region exhibits much lower resistivity than the surrounding MAPbI$_3$; thus, similarly forming conductive clusters.[12,45] The detailed mechanism of the resistive switching in our devices is further explained in Section S8, Supporting Information.

The memory performance was characterized in terms of retention and endurance characteristics (Figure 2b,c). The perovskite memory devices showed a retention time of more than 1000 s under 0.05 V bias (Figure 2b), which is small enough to avoid unintentional switching. It could be driven more than 100 cycles (Figure 2c).

The perovskite memory devices showed different IRSs by controlling the compliance current (**Figure 3**a). In each resistance state, current noise was measured when applying a small voltage (0.1 V) where resistive switching would not occur. The measurement setup can be found in Figure S3, Supporting Information. Figure 3b shows the current noise amplitude (S_I, spectral noise power density) as a function of frequency for four resistance states, indicating that low-frequency $1/f$ type noise characteristics were observed in the frequency range between 10 and 1500 Hz for each resistance state. As shown in Figure 3b, the magnitude of S_I increases as the resistance value of the state increases.

Figure 3c shows the normalized current noise power spectral density (S_I/I^2; hereafter denoted as normalized current noise) measured at 998.4 Hz in each IRS. The scaling behavior was observed according to the power-law between the S_I/I^2 and resistance values. Such a scaling behavior can be attributed to the formation of percolation paths within the material.[37,46,47] According to the percolation theory, a resistive switching medium is a network consisting of conducting and insulating fractions. A percolation path between the two electrodes is formed when the conductive volume fraction (ϕ) increases and reaches a certain threshold (critical conductive volume fraction, ϕ_c). Here, the noise of the entire system is

ADVANCED
SCIENCE NEWS
www.advancedsciencenews.com

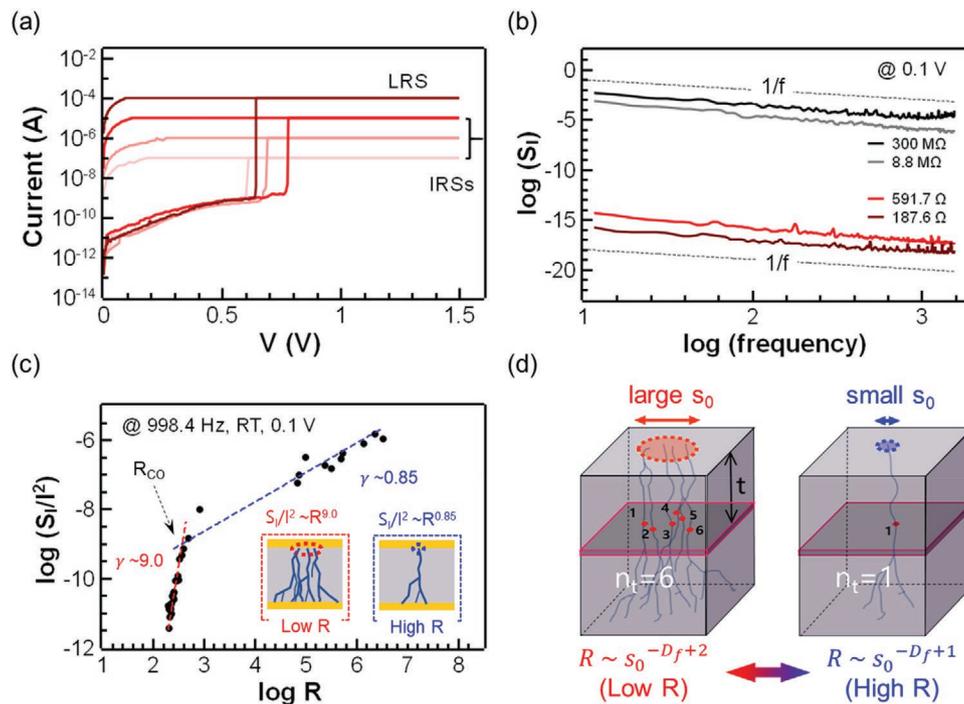ADVANCED
FUNCTIONAL
MATERIALS
www.afm-journal.de

Figure 3. a) Current-voltage curves of a perovskite resistive memory device measured at room temperature showing LRS and various IRSs. b) Spectral noise power density (S_I) versus frequency for four resistance states showing low-frequency $1/f$ noise characteristics. c) Normalized current noise power spectral density (S_I/I^2) for various resistance states showing a crossover behavior at about 400 Ω. d) Schematics of conducting filaments with fractal geometry. The number of current paths (cases of $n_t = 6$ and $n_t = 1$ are depicted) is shown on the cross-section at a distance t from the top electrode. The lateral size of the bottleneck structure (s_0) is closely related to the scaling crossover behavior.

mainly determined by the smallest bottleneck region of the percolative path, where the electric field and current density are the most concentrated. The noise decreases as a power law as the number of current paths increases, decreasing the resistance of the total network.[48,49] It means that the following relationship is satisfied between the total resistance (R) and normalized current noise.

$$\frac{S_I}{I^2} \propto R^{\gamma} \tag{1}$$

when $\phi > \phi_c$. Here, ϕ is conductive volume fraction and ϕ_c is critical conductive volume fraction. Note that the observed power law of the scaling behavior suggests that the resistive switching of our MAPbI$_3$ memory device is governed by the percolative conducting filament in the bulk rather than a homogeneous switching by interfacial effect.

The two scaling regimes depending on the resistance appeared: $\frac{S_I}{I^2} \propto R^{9.0}$ for $R < R_{co}$ and $\frac{S_I}{I^2} \propto R^{0.85}$ for $R > R_{co}$. Here, R_{co} is the resistance at which scaling exponent crossover occurred (marked as an arrow in Figure 3c) and was found to be about 400 Ω. Similar crossover behaviors with two scaling regimes were observed in the oxide-based unipolar resistive memory.[50,51] To investigate this scaling crossover, a model of a percolating cluster with fractal geometry was proposed.[52] The total resistance and normalized noise are closely related to the current distribution in the system; both quantities depend on the interconnection within the conducting network.[48,53] They

can be expressed in terms of n_t, which stands for the number of current paths at distance t from the origin (top electrode in this study, schematically shown in Figure 3d). It is known that n_t satisfies the relationship: $n_t \propto t^{D_{(t)}-1}$ for a fractal structure.[54,55] Here, D_f is the fractal dimension of the filament structure. Fractal is a mathematical object that exhibits self-similarity, and a fractal dimension derived from the scaling relation of a structure is an indicator of the complexity. An object with a large fractal dimension has a complex structure, and it densely fills the embedded space. The fractal dimension of the conducting filaments can be obtained using the scaling behavior between the normalized noise magnitudes and total resistance for each state. Another important parameter for explaining the scaling crossover is the lateral size of the bottleneck (s_0) where the current is most concentrated. From the fractal geometry, the following relationship can be used:

$$n_t \approx (s_0 + t)^{D_f - 1} \tag{2}$$

Scaling relationships for total resistance and normalized noise magnitude are divided into two regions according to the size of s_0, thus scaling exponent (γ) in Equation (1) changes at a certain threshold of s_0 (see Figure 3d).[52,56]

$$\gamma = \frac{D_f}{D_f - 2} \text{ for } R < R_{co} \text{ and } \gamma = 1 \text{ for } R > R_{co} \tag{3}$$

The fractal dimension of conducting filaments in perovskite was best fitted to be about 2.25. This value is similar to
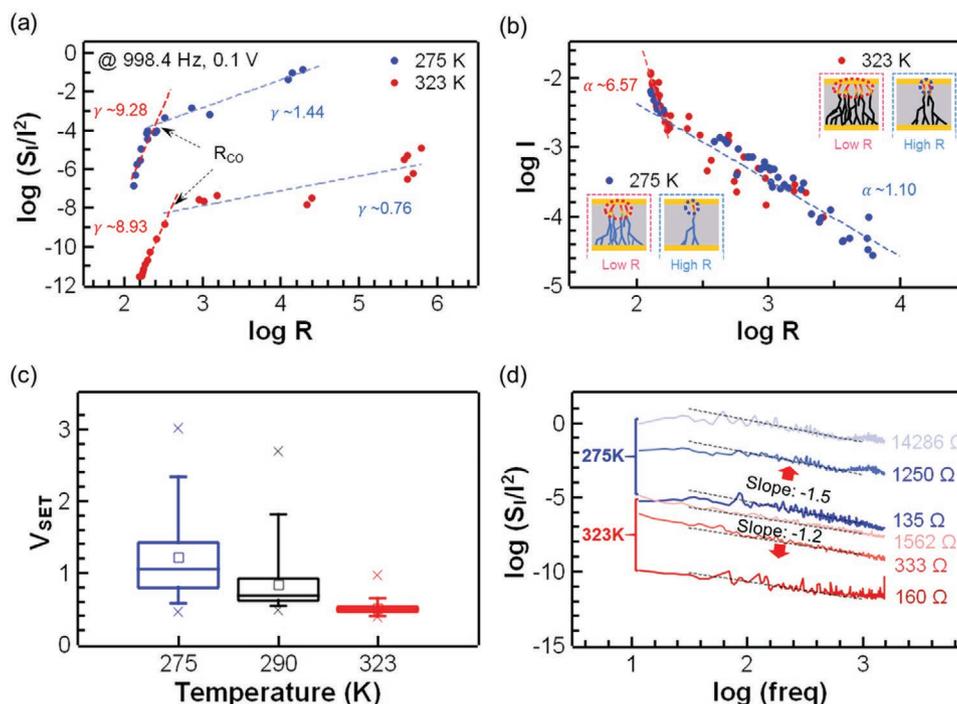
Figure 4. a) Normalized current noise power spectral density versus the resistance of a perovskite resistive memory device at 275 (blue symbols) and 323 K (red symbols). b) Reset current versus resistance at 275 (blue symbols) and 323 K (red symbols) showing scaling crossover behavior. Insets show schematics of conducting filaments and the hottest bottleneck region (dotted circles in red) at each temperature. c) Distribution of the set voltage during the 50 cycles of set/reset operation at 275, 290, and 323 K (each depicted in blue, black, red box diagram, respectively). d) Normalized noise spectra in a frequency domain measured at 275 (blue lines) and 323 K (red lines).

(and slightly smaller than) that reported in a previous study for metal oxide thin film-based resistive memory ($D_f \approx 2.54$),[52] suggesting that a relatively simple conducting filament structure has been formed. A smaller fractal dimension of 2.25 might be related to the formation of conducting filaments around the grain boundaries, where the ion migration is frequent in organometal perovskite.[57]

The ion migration responsible for the formation of conductive clusters in organometal perovskite is expected to occur more readily at higher temperatures.[58] Therefore, the structure of conducting filaments discussed above is expected to vary with temperature. **Figure 4**a shows the magnitude of normalized current noise at 998.4 Hz in each IRS measured at two temperatures (275 and 323 K). As shown in Figure 3c (measured at room temperature), the scaling behavior also showed the crossover at R_{co} of about 400 Ω at 275 and 323 K (Figure 4a). Compared with the results at room temperature (Figure 3c), the scaling exponents have similar values in $R > R_{co}$ and $R < R_{co}$ regions among the three temperatures, which also indicates a similar fractal dimension ($D_f \approx 2.25$). However, the scaling exponent tended to slightly increase as the temperature decreases. This is presumably because the magnitude of elementary fluctuations from the material constituting the conducting filaments increases as temperature decreases. Accordingly, the effect of normalized noise magnitude over total resistance increases to modify the scaling exponents. The most distinct difference in the noise scaling at high and low temperatures was the noise magnitude. The magnitude of the normalized noise at high temperature is similar to that of

room temperature; however, four to five orders of magnitude are larger in the low-temperature case, suggesting that the current fluctuation of conducting filaments at low temperature is relatively large.

To further support the percolation-scaling behavior and related fractal structure of the conducting filaments, reset current, which is the maximum current value before the reset occurs, was plotted as a function of resistance (called "I-R scaling") in Figure 4b. Similarly, two scaling regimes were observed in the I-R scaling. The I-R scaling behavior can also be explained by the same percolation model with fractal geometry. According to the model proposed by Lee et al., the change in the scaling exponent across the crossover occurs based on the area of the bottleneck region, where the current is the most concentrated among the conducting filaments (see inset of Figure 4b). During the reset process, the bottleneck area through which the largest current flows becomes the hottest region in the entire conducting network due to Joule heating. When the temperature of the bottleneck area exceeds the critical temperature, even if the remaining filament structure is maintained, the bottleneck region of the filament is ruptured, and the resistance state of the memory device is switched to HRS. The heat conduction and dissipation that occur during such a reset event can be simulated based on the heat equation using the finite element method. As a result, the minimum heat required to raise the temperature of the bottleneck region to the critical temperature exhibits a power-law relationship with the cross-sectional area of the bottleneck region (see Section S5, Supporting Information). The scaling theory predicts that the

**ADVANCED
SCIENCE NEWS**
www.advancedsciencenews.com

**ADVANCED
FUNCTIONAL
MATERIALS**
www.afm-journal.de

exponent for reset current scaling (α) and resistance satisfies the following relationship.[52]

$$I_{Reset} \approx R^{-\alpha} \tag{4}$$

$$\alpha = \frac{D_f - \beta + 1}{2(D_f - 2)} \text{ (for } R < R_{co}) \text{ and } \alpha = \frac{D_f - \beta + 1}{2(D_f - 1)} \text{ (for } R > R_{co}) \tag{5}$$

From the simulation, the β value was calculated to be 0.33 for the MAPbI$_3$. The extracted scaling exponents were 6.57 and 1.10 in $R < R_{co}$ and $R > R_{co}$ regions, respectively. Accordingly, D_f value of the conducting filament was calculated to be about 2.2, which matches well with the fractal dimension estimated by the noise scaling, supporting the validity of the proposed fractal geometry model of the filamentary paths.

The temperature-dependent ion migration process is expected to be apparent from the memory operation characteristics, especially the set and reset characteristics of the perovskite memory devices. Figure 4c shows the distribution of the set voltage during the 50 cycles of the set/reset operation at each temperature for the same device. The set process is the result of electric field-driven vacancy migration toward the conducting filament. Therefore, the set voltage decreases at a high temperature where ion migration is active, which is consistent with our experimental results in Figure 4c. Additionally, the set voltage distribution becomes narrower as the temperature increases. Although the temperature dependence of the set voltage magnitude can be explained by the ion migration picture, predicting the temperature dependence of the set voltage distribution is nontrivial. As previously mentioned, conducting filaments formed are not completely dissociated during the reset process but are ruptured only in the bottleneck region where the current is the most concentrated. Then, the remaining filament structure affects the subsequent set processes since it concentrates electric field. Thus, it gives spatial confinement to filament growth. As more parts of the structure remain (i.e., the ruptured gap of the conducting filament becomes smaller), the subsequent set voltage distribution becomes narrower.[59,60] Previous studies using numerical simulations have reported a robust filamentary structure with relatively large lateral size leaves rather than a small gap during the rupture process.[19,22] Therefore, it can be inferred that in our experiments, a more robust filamentary structure with numerous current paths was formed at LRS of 323 K than that of 290 and 275 K.

Figure 4d shows a comparison of normalized noise spectra in a frequency domain of the same device measured at 275 and 323 K. There are differences in the results measured at different temperatures. The noise magnitude level was four to five orders of magnitude larger at 275 K than that of 323 K, even though they have similar resistance. It means that the current fluctuation was relatively larger in the 275 K case. The slope of $1/f$ type noise at high temperature fits well to about 1.2, but the slope at low temperature best fits at about 1.5. As reported previously, the slope of $\approx$1.5 is often related to current fluctuations induced by diffusion/migration processes.[61–64] Such current fluctuations can be directly probed in the time domain, which will be the focus of the latter part of this study. This $1/f^{1.5}$ noise with a larger magnitude suggests that the underlying process of noise at IRSs of 275 K is different compared to 323 K or room

temperature cases. The measured temperature range was limited below 323K due to potential artifacts from the phase transition from tetragonal to cubic phase at $\approx$330 K.[65,66]

In order to examine the correlation between the larger slope of the noise spectra for lower temperature (Figure 4d) and current fluctuations, we collected the current time trace data for various resistance states accessible in our perovskite memory devices. The time trace data were collected by applying a small bias (0.05 V) (see Figure S3, Supporting Information, for the measurement setup). As shown in **Figure 5**a, the current trace in the IRS states at low-temperature conditions (275 K) showed step-like fluctuations, which is a typical feature of random telegraph noise (RTN). The RTN features were observed for the IRSs with higher resistance values (bottom three panels of Figure 5a) whereas the lowest resistance states (top panel of Figure 5a) did not show any current fluctuations within the measured time range. Similar current fluctuations have previously been associated with processes such as charge trapping/de-trapping at the defects close to the conducting filaments or current fluctuations induced by diffusion/migration of ions, which provided a mechanistic picture towards understanding resistive switching mechanisms in various material-based memory systems.[47,63,64,67–69] Therefore, we proceeded with a detailed analysis of the observed current fluctuations in our perovskite memory devices for the different resistance states by visually representing the distribution of the current levels in the time trace as current histograms (Figure 5b). From the histograms collected from the time trace data over a period of 0.1 s, we can extract the discrete current levels among which the fluctuations occur by determining the major peaks. We can verify that the discrete current levels are distributed over about an order of magnitude in current for the IRSs (three bottom panels in Figure 5b), whereas the LRS shows a single major current peak (top panel in Figure 5b). This is also reflected in the time trace data in Figure 5a where the LRS (140 Ω state) shows almost no current fluctuations, which can be related to stable and numerous current paths (see top panel in Figure 5c). On the other hand, the large current fluctuations in the IRSs spanned over the cross-over current I_{co} of $\approx$200 μA (i.e., the current at R_{co}, see Figure 4a) where the bottleneck size of the conducting filaments is equal to the threshold bottleneck size s_{co} (= s_0 at R_{co}, see Figure 3c,d).

Since each major peak in the current histogram corresponds to a possible configuration of conducting filaments, the existence of multiple major peaks in our current histogram (Figure 5b) suggests that the resistive switching in our perovskite memory devices involves multi-level transitions (see Section S6, Supporting Information) like in organic nanocomposite memory devices.[47,64] Furthermore, we can identify the underlying configurational relationships between the different IRSs by comparing the peak positions of these multi-current levels from the current histograms. We suggest that the formed percolative conducting paths in different resistance states are not completely random but have a common configuration to some degree. Specifically, we can observe common current level peaks near $\approx$245 and $\approx$270 μA (indicated with red dashed lines) for both the 250 and 830 Ω states (middle two panels in Figure 5b). Also, we can find common current levels in the range of $\approx$20 to $\approx$50 μA (indicated as a yellow box) for both the 830 and 1250 Ω states (bottom
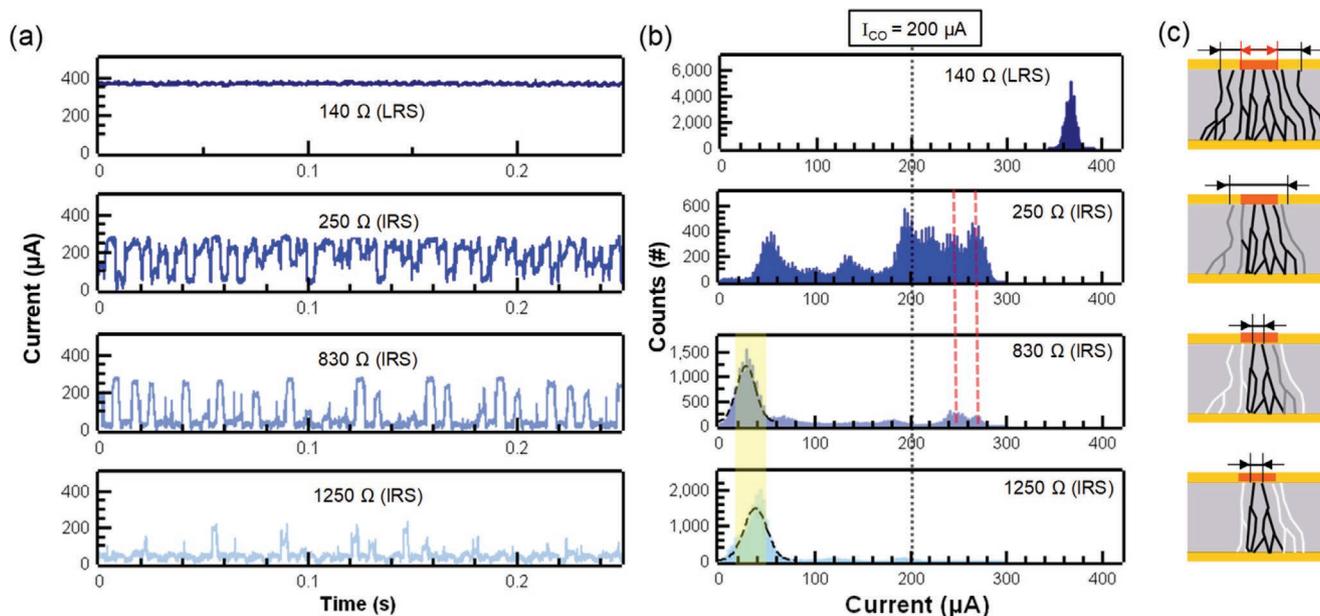
Figure 5. a) Current time trace for various resistance states measured at 275 K and b) corresponding current histogram for 0.1 s. RTN is exhibited in IRSs. Common current level peaks near ≈245 and ≈270 µA are indicated with red dashed lines. Common current level peaks located in the range of ≈20 to ≈50 µA (yellow box) are Gaussian-fitted. c) Schematic representation of fluctuations in conducting filaments at corresponding resistance states (see the text).

two panels in Figure 5b). However, the relative stability differs depending on the resistance state, which can be related to the relative frequency of each current peak in the histogram, accordingly. The higher current level peaks are more frequent in the LRSs, whereas the lower current level peaks are more frequent in the HRSs (Figure 5b).

Now, we propose an overall picture for summarizing the different configurations of local conducting filaments and their relative stability based on our previous discussions. The number of conducting filament branches is represented as an indicator for the average resistance of the resistance state (Figure 5c); the larger the number of the conducting filament branches, the lower the average resistance. The conducting filament branches are expressed in different colors; black, gray, and white filaments indicate stable, less stable, and the least stable paths, respectively. The origin of the multiple current peaks in the current histogram observed for the IRSs (Figure 5b) is depicted as the current fluctuation induced by the formation and dissolution of unstable conducting filament branches. The sizes of the bottleneck (s_0) are expressed as black arrows with respect to the threshold bottleneck size (s_{co}) expressed as red arrows. The number of stable conducting filaments and the size of bottleneck regions decrease as the average resistance of the state increases (Figure 5c and also see Figure 3d). Furthermore, the physical origin of the current fluctuation in our perovskite memory devices is presumed to be due to the local change in the structure of conducting filaments induced by ion migration processes. This is consistent with the disappearance of the RTN at a high temperature (323 K) (see Figure S7, Supporting Information), indicating a relatively small contribution of local unstable current paths toward the total current due to a more active ion migration at higher temperatures. Accordingly, although this is beyond the scope of our study, the conducting filaments are expected to be more stable in the cubic phase (above 330K) than in the tetragonal phase (this work) due to a lower activation energy for ion migration.[70–72]

3. Conclusion

In this study, we investigated the electrical properties of resistive memory devices made with MAPbI$_3$ organometal perovskite. We adopted the current noise analysis as a simple and non-invasive tool to investigate the characteristics of conducting filaments in perovskite memory. By applying the percolation model with fractal geometry, we explained the scaling crossover behaviors in the normalized current noise and reset current. Additionally, by measuring the current noise at different temperatures, we observed the alteration of current levels in IRSs under low-temperature (275 K) conditions and a single peak distribution of current values at high temperature (323 K). We suggest that stable and robust filaments are formed under elevated-temperature conditions where ion migration is more active, resulting in stable multilevel operations with less noise. Our work demonstrates that the employed noise analysis can be a powerful tool for revealing the resistive switching mechanism in organo-metal-halide perovskites, which can be expanded to other perovskite materials including all-inorganic perovskites for enhancing the operation stability in multi-state perovskite memory devices.

4. Experimental Section

Device Fabrication: Organometal perovskite resistive memory devices were fabricated as previously described.[15] Ti/Au bottom electrodes with line widths of 50 µm were deposited on the Si/SiO$_2$ substrate by

electron beam evaporation through a shadow mask. First, 5 nm-thick Ti, which serves as an adhesive layer, was deposited, followed by 50 nm-thick Au. The substrate with the bottom electrodes was treated with UV-ozone (15 min) to enhance the film quality of the spin-coated MAPbI$_3$. MAI and PbAc$_2$ were dissolved by 3:1 in a molar ratio in N, N-dimethylformamide to form a 0.63 M solution. MAI and PbAc$_2$ were purchased from Dyesol (CAS#: 14965-49-2) and Sigma-Aldrich (CAS#: 6080-56-4), respectively. The solution was stirred at 60 °C for 30 min, then spin-coated onto the substrate in an N$_2$-filled glove box at a rate of 5000 rpm for 45 s. After the spin-coating, the samples were air-dried for 10 min and soft-baked at 100 °C for 5 min. Top electrodes (50 nm-thick Au) were deposited through a shadow mask of line-width 50 μm by electron beam evaporation.

Device Characterization: The electrical measurements were performed using a semiconductor parameter analyzer (Keithley 4200 SCS) and a probe station system (JANIS ST-500) in a vacuum environment (≈10^{-5} Torr). The voltage sweep rate in I–V measurements was 0.54 V s^{-1}. The bottom electrode was grounded, and a voltage was applied to the top electrode.

For the noise measurement, a low-noise current amplifier (Ithaco 1211) was used for converting the current noise signal into an amplified voltage signal. The signal was measured in the frequency domain using a spectrum analyzer (Stanford Research SR760) and in the time domain using a ground-isolated 16-bit analog-digital converter (ADC). A 16-bit digital-analog converter (DAC) controlled by a LABVIEW was used to apply a voltage. A digital multimeter (Agilent 34401A) was used to measure the average current.

Thermal Simulation: To estimate the exponent β in Equation (5), a numerical simulation for heat dissipation was performed through the organometal perovskite device. Figure S5a, Supporting Information, shows the simulation setup for the MAPbI$_3$ device, which was a 3D cylindrical structure with a radius of 1 μm. The MAPbI$_3$ layer with a thickness of 200 nm was sandwiched by 50 nm-thick Au bottom and top electrodes on a 270 nm-thick SiO$_2$ substrate. The top electrode was covered by a 400 nm-thick air layer. A cylindrical conducting filament with a radius of s nm was located at the center inside the MAPbI$_3$ layer. For simplicity, the fractal structure of the conducting filament was not considered in this simulation. With this setup, the heat equation

$$\rho C_p \frac{dT(\vec{r})}{dt} = k\,\nabla^2 T(\vec{r}) + q(\vec{r}) \tag{6}$$

was numerically solved for calculating the temperature profile of the device using the finite element method with a mesh size of 2 nm. In Equation (6), ρ, C_p, k, and $q(\vec{r})$ are the density, specific heat, thermal conductivity, and heat power, respectively. A detailed description of the simulation, including the parameters used for the simulation, can be found in Section S5, Supporting Information.

Supporting Information

Supporting Information is available from the Wiley Online Library or from the author.

Acknowledgements

Conflict of Interest

The authors declare no conflict of interest.

Data Availability Statement

Research data are not shared.

Keywords

[1] M. Grätzel, *Nat. Mater.* **2014**, *13*, 838.
[2] T. M. Brenner, D. A. Egger, L. Kronik, G. Hodes, D. Cahen, *Nat. Rev. Mater.* **2016**, *1*, 15007.
[3] W. Nie, H. Tsai, R. Asadpour, J.-C. Blancon, A. J. Neukirch, G. Gupta, J. J. Crochet, M. Chhowalla, S. Tretiak, M. A. Alam, H.-L. Wang, A. D. Mohite, *Science* **2015**, *347*, 522.
[4] Z.-K. Tan, R. S. Moghaddam, M. L. Lai, P. Docampo, R. Higler, F. Deschler, M. Price, A. Sadhanala, L. M. Pazos, D. Credgington, F. Hanusch, T. Bein, H. J. Snaith, R. H. Friend, *Nat. Nanotechnol.* **2014**, *9*, 687.
[5] S. D. Stranks, H. J. Snaith, *Nat. Nanotechnol.* **2015**, *10*, 391.
[6] J. Choi, J. S. Han, K. Hong, S. Y. Kim, H. W. Jang, *Adv. Mater.* **2018**, *30*, 1704002.
[7] S. P. Senanayak, M. Abdi-Jalebi, V. S. Kamboj, R. Carey, R. Shivanna, T. Tian, G. Schweicher, J. Wang, N. Giesbrecht, D. Di Nuzzo, H. E. Beere, P. Docampo, D. A. Ritchie, D. Fairen-Jimenez, R. H. Friend, H. Sirringhaus, *Sci. Adv.* **2020**, *6*, eaaz4948.
[8] E. J. Yoo, M. Lyu, J. H. Yun, C. J. Kang, Y. J. Choi, L. Wang, *Adv. Mater.* **2015**, *27*, 6170.
[9] J. Choi, S. Park, J. Lee, K. Hong, D. H. Kim, C. W. Moon, G. D. Park, J. Suh, J. Hwang, S. Y. Kim, H. S. Jung, N.-G. Park, S. Han, K. T. Nam, H. W. Jang, *Adv. Mater.* **2016**, *28*, 6562.
[10] C. Gu, J.-S. Lee, *ACS Nano* **2016**, *10*, 5413.
[11] J. Choi, Q. V. Le, K. Hong, C. W. Moon, J. S. Han, K. C. Kwon, P.-R. Cha, Y. Kwon, S. Y. Kim, H. W. Jang, *ACS Appl. Mater. Interfaces* **2017**, *9*, 30764.
[12] X. Zhu, J. Lee, W. D. Lu, *Adv. Mater.* **2017**, *29*, 1700527.
[13] K. Yan, M. Peng, X. Yu, X. Cai, S. Chen, H. Hu, B. Chen, X. Gao, B. Dong, D. Zou, *J. Mater. Chem. C* **2016**, *4*, 1375.
[14] J. Liu, J. Jin, Z. Yang, J. Cai, J. Yue, J. Impundu, H. Liu, H. Wei, Z. Peng, Y. J. Li, L. Sun, *ACS Appl. Mater. Interfaces* **2020**, *12*, 31776.
[15] K. Kang, H. Ahn, Y. Song, W. Lee, J. Kim, Y. Kim, D. Yoo, T. Lee, *Adv. Mater.* **2019**, *31*, 1804841.
[16] R. Waser, M. Aono, *Nat. Mater.* **2007**, *6*, 833.
[17] T. Lee, Y. Chen, *MRS Bull.* **2012**, *37*, 144.
[18] B. Hwang, C. Gu, D. Lee, J. S. Lee, *Sci. Rep.* **2017**, *7*, 43794.

[19] Y. Huang, L. Tang, C. Wang, H. Fan, Z. Zhao, H. Wu, M. Xu, R. Shen, Y. Yang, J. Bian, *ACS Appl. Electron. Mater.* **2020**, *2*, 3695.

[20] X. Zhao, Z. Wang, W. Li, S. Sun, H. Xu, P. Zhou, J. Xu, Y. Lin, Y. Liu, *Adv. Funct. Mater.* **2020**, *30*, 1910151.

[21] C. Eames, J. M. Frost, P. R. Barnes, B. C. O'regan, A. Walsh, M. S. Islam, *Nat. Commun.* **2015**, *6*, 7497.

[22] Y.-H. Sun, Y. Huang, L.-Z. Tang, C. Wang, presented at *2020 IEEE 15th Int. Conf. on Solid-State & Integrated Circuit Technology (ICSICT)*, Kunming, November **2020**.

[23] S. Lee, H. Kim, D. H. Kim, W. B. Kim, J. M. Lee, J. Choi, H. Shin, G. S. Han, H. W. Jang, H. S. Jung, *ACS Appl. Mater. Interfaces* **2020**, *12*, 17039.

[24] J. Spring, E. Sediva, Z. D. Hood, J. C. Gonzalez-Rosillo, W. O'Leary, K. J. Kim, A. J. Carrillo, J. L. M. Rupp, *Small* **2020**, *16*, 2003224.

[25] S. Choi, S. H. Tan, Z. Li, Y. Kim, C. Choi, P.-Y. Chen, H. Yeon, S. Yu, J. Kim, *Nat. Mater.* **2018**, *17*, 335.

[26] J. Yao, Z. Sun, L. Zhong, D. Natelson, J. M. Tour, *Nano Lett.* **2010**, *10*, 4105.

[27] D.-H. Kwon, K. M. Kim, J. H. Jang, J. M. Jeon, M. H. Lee, G. H. Kim, X.-S. Li, G.-S. Park, B. Lee, S. Han, M. Kim, C. S. Hwang, *Nat. Nanotechnol.* **2010**, *5*, 148.

[28] J.-Y. Chen, C.-L. Hsin, C.-W. Huang, C.-H. Chiu, Y.-T. Huang, S.-J. Lin, W.-W. Wu, L.-J. Chen, *Nano Lett.* **2013**, *13*, 3671.

[29] I. K. Yoo, B. S. Kang, S. E. Ahn, C. B. Lee, M. J. Lee, G.-S. Park, X.-S. Li, *IEEE Trans. Nanotechnol.* **2010**, *9*, 131.

[30] U. Celano, L. Goux, A. Belmonte, K. Opsomer, A. Franquet, A. Schulze, C. Detavernier, O. Richard, H. Bender, M. Jurczak, W. Vandervorst, *Nano Lett.* **2014**, *14*, 2401.

[31] J. S. Lee, S. Lee, T. W. Noh, *Appl. Phys. Rev.* **2015**, *2*, 031303.

[32] S. Kogan, *Electronic noise and fluctuations in solids*, Cambridge University Press, Cambridge **2008**.

[33] Y. Song, T. Lee, *J. Mater. Chem. C* **2017**, *5*, 7123.

[34] T. Nagumo, K. Takeuchi, S. Yokogawa, K. Imai, Y. Hayashi, presented at *2009 IEEE Int. Electron Devices Meeting (IEDM)*, Baltimore, December **2009**.

[35] J. Park, D. Kang, J.-K. Son, H. Shin, *IEEE Trans. Electron Devices* **2012**, *59*, 3495.

[36] R. Rammal, A. Tremblay, *Phys. Rev. Lett.* **1987**, *58*, 415.

[37] S. B. Lee, S. Park, J. S. Lee, S. C. Chae, S. H. Chang, M. H. Jung, Y. Jo, B. Kahng, B. S. Kang, M.-J. Lee, T. W. Noh, *Appl. Phys. Lett.* **2009**, *95*, 122112.

[38] T. J. Jacobsson, L. J. Schwan, M. Ottosson, A. Hagfeldt, T. Edvinsson, *Inorg. Chem.* **2015**, *54*, 10678.

[39] W. Zhang, M. Saliba, D. T. Moore, S. K. Pathak, M. T. Hörantner, T. Stergiopoulos, S. D. Stranks, G. E. Eperon, J. A. Alexander-Webber, A. Abate, A. Sadhanala, S. Yao, Y. Chen, R. H. Friend, L. A. Estroff, U. Wiesner, H. J. Snaith, *Nat. Commun.* **2015**, *6*, 6142.

[40] P. Zaumseil, *J. Appl. Crystallogr.* **2015**, *48*, 528.

[41] K. Uosaki, Y. Shen, T. Kondo, *J. Phys. Chem.* **1995**, *99*, 14117.

[42] D. S. Jeong, R. Thomas, R. S. Katiyar, J. F. Scott, H. Kohlstedt, A. Petraru, C. S. Hwang, *Rep. Prog. Phys.* **2012**, *75*, 076502.

[43] J. H. Yoon, J. H. Han, J. S. Jung, W. Jeon, G. H. Kim, S. J. Song, J. Y. Seok, K. J. Yoon, M. H. Lee, C. S. Hwang, *Adv. Mater.* **2013**, *25*, 1987.

[44] I. H. Inoue, S. Yasuda, H. Akinaga, H. Takagi, *Phys. Rev. B* **2008**, *77*, 035105.

[45] W.-J. Yin, T. Shi, Y. Yan, *Appl. Phys. Lett.* **2014**, *104*, 063903.

[46] J. Planès, A. François, *Phys. Rev. B* **2004**, *70*, 184203.

[47] Y. Song, H. Jeong, J. Jang, T.-Y. Kim, D. Yoo, Y. Kim, H. Jeong, T. Lee, *ACS Nano* **2015**, *9*, 7697.

[48] R. Rammal, C. Tannous, P. Breton, A. Tremblay, *Phys. Rev. Lett.* **1985**, *54*, 1718.

[49] R. Rammal, C. Tannous, A. Tremblay, *Phys. Rev. A* **1985**, *31*, 2662.

[50] S. B. Lee, S. C. Chae, S. H. Chang, J. S. Lee, S. Seo, B. Kahng, T. W. Noh, *Appl. Phys. Lett.* **2008**, *93*, 212105.

[51] Z. Q. Wang, X. H. Li, H. Y. Xu, W. Wang, H. Yu, X. T. Zhang, Y. X. Liu, Y. C. Liu, *J. Phys. D: Appl. Phys.* **2010**, *43*, 385105.

[52] J. S. Lee, S. B. Lee, S. H. Chang, L. G. Gao, B. S. Kang, M. J. Lee, C. J. Kim, T. W. Noh, B. Kahng, *Phys. Rev. Lett.* **2010**, *105*, 205701.

[53] M. A. Dubson, Y. C. Hui, M. B. Weissman, J. C. Garland, *Phys. Rev. B* **1989**, *39*, 6807.

[54] L. Niemeyer, L. Pietronero, H. J. Wiesmann, *Phys. Rev. Lett.* **1984**, *52*, 1033.

[55] D. Ben-Avraham, S. Havlin, *Diffusion and Reactions in Fractals and Disordered Systems*, Cambridge University Press, Cambridge **2000**.

[56] Y. Yagil, G. Deutscher, *Phys. Rev. B* **1992**, *46*, 16115.

[57] Y. Shao, Y. Fang, T. Li, Q. Wang, Q. Dong, Y. Deng, Y. Yuan, H. Wei, M. Wang, A. Gruverman, J. Shield, J. Huang, *Energy Environ. Sci.* **2016**, *9*, 1752.

[58] J. Xing, Q. Wang, Q. Dong, Y. Yuan, Y. Fang, J. Huang, *Phys. Chem. Chem. Phys.* **2016**, *18*, 30484.

[59] S. C. Chae, J. S. Lee, S. Kim, S. B. Lee, S. H. Chang, C. Liu, B. Kahng, H. Shin, D.-W. Kim, C. U. Jung, S. Seo, M.-J. Lee, T. W. Noh, *Adv. Mater.* **2008**, *20*, 1154.

[60] Q.-Q. Sun, J.-J. Gu, L. Chen, P. Zhou, P.-F. Wang, S.-J. Ding, D. W. Zhang, *IEEE Electron Device Lett.* **2011**, *32*, 1167.

[61] K. Van Vliet, H. Mehta, *Phys. Status Solidi B* **1981**, *106*, 11.

[62] P. R. F. Rocha, H. L. Gomes, L. K. J. Vandamme, Q. Chen, A. Kiazadeh, D. M. De Leeuw, S. C. J. Meskers, *IEEE Trans. Electron Devices* **2012**, *59*, 2483.

[63] N. Raghavan, D. D. Frey, K. L. Pey, *Microelectron. Reliab.* **2014**, *54*, 1729.

[64] Y. Song, H. Jeong, S. Chung, G. H. Ahn, T. Y. Kim, J. Jang, D. Yoo, H. Jeong, A. Javey, T. Lee, *Sci. Rep.* **2016**, *6*, 33967.

[65] P. S. Whitfield, N. Herron, W. E. Guise, K. Page, Y. Q. Cheng, I. Millas, M. K. Crawford, *Sci. Rep.* **2016**, *6*, 35685.

[66] C. Quarti, E. Mosconi, J. M. Ball, V. D'Innocenzo, C. Tao, S. Pathak, H. J. Snaith, A. Petrozza, F. De Angelis, *Energy Environ. Sci.* **2016**, *9*, 155.

[67] S. Ambrogio, S. Balatti, A. Cubeta, A. Calderoni, N. Ramaswamy, D. Ielmini, presented at *2013 IEEE Int. Electron Devices Meeting (IEDM)*, Washington, December **2013**.

[68] S. Choi, Y. Yang, W. Lu, *Nanoscale* **2014**, *6*, 400.

[69] Y. Zhang, H. Wu, M. Wu, N. Deng, Z. Yu, J. Zhang, H. Qian, *Appl. Phys. Lett.* **2014**, *104*, 103507.

[70] M. H. Futscher, J. M. Lee, L. McGovern, L. A. Muscarella, T. Wang, M. I. Haider, A. Fakharuddin, L. S. Mende, B. Ehrler, *Mater. Horiz.* **2019**, *6*, 1497.

[71] Y. Yuan, J. Huang, *Acc. Chem. Res.* **2016**, *49*, 286.

[72] W. A. Saidi, J. J. Choi, *J. Chem. Phys.* **2016**, *145*, 144702.